Efficient noise footprint computation for urban air mobility maneuvers in vertiport environments

Yunus, F.; Varriale, Carmine; Snellen, M.

DOI
10.2514/6.2024-3335

Publication date
2024

Document Version
Final published version

Published in
30th AIAA/CEAS Aeroacoustics Conference (2024)

Aeroacoustics Conferences
June 4-7, 2024, Rome, Italy
30th AIAA/CEAS Aeroacoustics Conference (2024)

10.2514/6.2024-3335

Efficient noise footprint computation for urban air mobility maneuvers in vertiport environments

Furkat Yunus *, Carmine Varriale †, and Mirjam Snellen ‡
Delft University of Technology, Faculty of Aerospace Engineering, Delft, The Netherlands

This paper introduces a methodology for predicting the noise footprint of urban air mobility (UAM) vehicles in vertiport environments during approach and departure maneuvers. The methodology integrates a flight mechanics model, an aerodynamic model, aeroacoustic models, and a noise propagation model. The flight mechanics model employs a point-mass dynamic model to determine optimal trajectories based on prescribed criteria. The aerodynamic model utilizes blade element momentum theory, while aeroacoustic models include frequency-domain acoustic formulation and a noise propagation model based on Gaussian beam propagation method, which accounts for 3D variations in terrain and atmospheric profiles. Noise footprints are computed for several waypoints, featuring significant variations in vehicle flight speed and pitch angle, and are subsequently compared. It is observed that variations in vehicle pitch angle significantly influence noise radiation directivity. Specifically, when the vehicle pitches up, on-ground noise levels beneath the source increase, while those at receivers farther away decrease. Conversely, when the vehicle pitches down, on-ground noise levels beneath the source decrease, while those at receivers farther away increase. Additionally, as flight speed increases, on-ground noise levels rise accordingly regardless of whether the vehicle pitches up or down. This trend suggests that lower flight speeds during approach and departure maneuvers are desirable to reduce the noise footprint. Furthermore, it is noted that building blocks further shield incoming noise and decrease noise levels at receivers distributed behind them. These findings underscore the necessity of the proposed approach in evaluating the noise footprint of UAM flight trajectories in vertiport environments, providing valuable insights for early design stages.

Nomenclature

α_{disk}	propeller disk angle of attack
α_b	local angle of attack at a blade section
α_f	fuselage pitch angle
β	blade twist angle
$\boldsymbol{x}$	receiver position vector with (x, y, z) components
Δr	width of a blade element
$\hat{\Psi}_{Fk}$	Frequency domain source function
Ω	rotor angular speed
ϕ	inflow induction angle
ϕ	tangential angle (z/y) and flow induction angle
ρ	air density
σ	rotor solidity
θ	receiver angle relative to flight direction, $\arccos(x/S)$
θ', ϕ'	angles θ and ϕ relative to propeller shaft axis
θ_{f}	fuselage pitch angle
θ_{tw}	normalized twist gradient
$\theta_{0.75}$	collective pitch angle
ξ	flight path angle
ζ	helix angle
a	axial velocity induction coefficient
A_{eq}	equivalent skin-friction area
B	number of blades

*Postdoctoral researcher, Aircraft Noise and Climate Effects section, Dept. of Control and Operations, f.yunus@tudelft.nl; AIAA Member
†Assistant Professor, Flight Performance and Propulsion section, Dept. of Flow Physics and Technology, c.varriale@tudelft.nl; AIAA Member
‡Professor, Aircraft Noise and Climate Effects section, Dept. of Control and Operations, m.snellen@tudelft.nl; AIAA Member

b	tangential velocity induction coefficient
b_c	blade sectional chord
B_D	chord to diameter ratio
c	sound speed
C_d	2D drag coefficient
C_l	2D lift coefficient
C_P	power coefficient
C_T	thrust coefficient
D	aerodynamic drag
h	altitude
I_y	lateral moment of inertia
J	advance ratio
$J_{mB-k}(x)$	Bessel function of order $mB-k$ and argument x
k	loading harmonic number
k_m	$\frac{mB\Omega}{c}$, harmonic wave number
k_x	dimensionless chordwise wave number
k_y	dimensionless spanwise wave number
L	aerodynamic lift
m	mass; and acoustic harmonic number
M_t	tip Mach number, $\Omega r_t/c$
M_x	flight Mach number, V/c
M_r	$\sqrt{M_x^2+M_t^2}$, helicoidal tip rotational Mach number
q	pitch rate
R	rotor radius; and radial position of a blade section
r_t	propeller tip radius
S	distance between propeller hub and receiver location, $\sqrt{x^2+y^2+z^2}$, m
T	thrust
t_b	thickness to chord ratio
u	aircraft longitudinal velocity
V	airspeed
w	aircraft normal velocity
w_{in}	rotor induced velocity
x_E	aircraft position
x_T	longitudinal position of thrust application point
z_0	non-dimensionalized blade radius, R/r_t
z_T	normal position of thrust application point
WP	waypoint

I. Introduction

A comprehensive evaluation of noise footprints resulting from takeoff and approach maneuvers executed by urban air mobility (UAM) vehicles, specifically electric vertical takeoff and landing (eVTOL) vehicles equipped with propeller propulsion, is crucial for facilitating the broad acceptance of UAM operations. This is particularly pertinent in the context of vertiports expected to be located in close proximity to residential areas. Vertiports, serving as nodes at the ends of airspace corridors, are identifiable ground or elevated locations exclusively designated for the takeoff and landing of eVTOL aircraft [1]. These eVTOL vehicles play a pivotal role in establishing connections between residential areas, airports, and city centers through UAM services.

While conducting takeoff, landing, and conversion flights near a vertiport, eVTOL vehicles experience pitch-up or pitch-down attitudes as they transition from one flight state (e.g., forward flight) to another (e.g., hover). During these maneuvers, the rotors operate at non-zero disk angle of attack α_{disk} (the angle between the local vertical and the thrust vector). In such scenarios, significant alterations in rotor noise emissions occure in comparison to operations at $\alpha_{disk} = 0^\circ$. These alterations lead to significant changes in noise footprints [2–8]. When a rotor operates at $\alpha_{disk} \neq 0^\circ$, two primary mechanisms contribute to rotor noise: periodic variations in blade loading (unsteady loading) and asymmetric phase modulation of noise sources' strength. The latter mechanism, also recognized as the wobbling mode [7, 9], is purely acoustic and characterized by the periodic variation of the observer-source relative Mach number. In this context, understanding how the noise footprint varies with changes in α_{disk}, which are directly influenced by pilot control inputs and operating conditions, is crucial. This understanding contributes to the determination of optimal flight procedures aimed at minimizing noise disturbance.

Recent years have witnessed a notable application of experimental and high-fidelity (HF) methodologies to investigate

the link between variations in α_{disk} and noise radiation patterns of propellers, both in the context of an isolated propeller [10, 11] and within the full vehicle configuration of an eVTOL vehicle [8, 12]. The investigation conducted by Romani et al. [10], for instance, examined the noise generated by a propeller at a non-zero α_{disk}, revealing that such configurations induce tonal loading noise propagation along the propeller axis. Furthermore, it is shown that non-zero α_{disk} can either amplify or attenuate noise levels in regions away from or toward which the propeller is tilted. Specifically, for low-speed propellers, the impact of acoustic modulation was deemed negligible, with noise variation primarily driven by unsteady loading effects. Similarly, Jatinder et al. [11] observed a similar trend in an isolated propeller, where loading noise increased in regions tilted away from the propeller and decreased in regions toward it. They noted that variations in the noise field were predominantly governed by unsteady loading effects, with the acoustic influence of α_{disk} being marginal, particularly at lower tip Mach numbers. Casalino et al. [8] investigated the sensitivity of noise footprints to variations in α_{disk} of tilt-rotors, among other parameters, in an eVTOL configuration. Three approach procedures with similar trajectories but varying aeromechanical trim settings were analyzed, revealing a substantial influence of tilt-rotor α_{disk} on overall noise levels across all trajectories. However, despite the invaluable insights provided by HF approaches into propeller noise emissions at non-zero α_{disk}, the integration of HF simulations into the assessment of low-noise flight trajectories is found to be cost-prohibitive, particularly in scenarios where thousands of noise spheres need computation, each representing the complex noise source directivity of the vehicle across various flight, operational, and environmental parameters, as observed in [8]. Consequently, the integration of high-fidelity approaches with design optimization processes to explore the acoustic impacts of flight and operational parameters on noise footprints is deemed impractical within an industrial context.

In contrast to HF approaches, low-order (LO) models have been developed and applied to study noise from rotors operating at non-zero α_{disk} [2, 3, 5, 7, 9, 13, 14]. Unlike HF approaches, which inherently account for the effects of unsteady loading and asymmetric phase modulation of steady noise sources, LO approaches address them in a two-step approach. In the first step, an aerodynamic model predicts the periodic variation of blade loading, serving as input for calculating noise due to unsteady loading. In the second step, analytical frequency domain formulations [3, 5, 9, 13], or Ffowcs Williams & Hawkings (FW-H) acoustic analogy, are employed to calculate noise due to asymmetric phase modulation, accounting for effects of non-zero α_{disk} with arbitrary direction both in time [15] and frequency [16] domains. These two steps are independent; hence, the significance of their contribution can be investigated independently. For instance, Hanson [3] demonstrated that the acoustic effect of non-zero α_{disk} is a dominant contributor to higher harmonics compared to the contribution from unsteady loading. Subsequently, Hanson [5] showed that the significance of change in noise levels is proportional to the increase in α_{disk}. Both of these trends are confirmed by recent work by the lead author [17], which compares results from a LO model that accounts only for the contribution due to asymetric phase modulation of source strength due to non-zero α_{disk} against outdoor measurements.

This study presents a methodology that integrates Hanson's frequency domain formulation [3], incorporating non-zero α_{disk} in acoustic calculations. The integration constitutes the original contribution of this work, incorporating models for flight mechanics, aerodynamics, aeroacoustics, noise propagation, and footprint calculation. Instantaneous noise footprints of realistic UAM vehicle flight trajectories are analyzed, focusing on the acoustic impact of variations in flight speed and α_{disk}. The investigation centers on the operation of a quadrotor vehicle in a vertiport environment within an urban area with high-rise buildings. This approach enables rapid calculation of noise footprints for flight procedures in a generic 3D environment, facilitating the identification of low-noise flight procedures that could minimize environmental noise impact on communities surrounding vertiports.

The paper is structured as follows. Methodology is outlined in Section II. In Section III, the noise footprint of a flight trajectory is examined in a case study, with specific attention to the acoustic effects influenced by variations in flight speed, α_{disk}, and vertiport geometry on the distribution of the noise footprint. Conclusions and future work are presented in Section IV.

II. Methodology

A standard hybrid approach is employed to calculate the noise footprint of a flight trajectory. In the first step, the flight trajectory to perform a specified maneuver in a time-optimal manner is calculated on the basis of top-level flight requirements (i.e., flight speed, altitude, etc.). In the second step, the necessary aerodynamic parameters (such as propeller rotational speed Ω, inflow velocity w_{in}, α_{disk}, and collective angle $\theta_{0.75}$) are extracted at a set of specified waypoints (WPs) to compute the corresponding aerodynamic forces on the propeller blade. This involves considering the propeller geometry and employing the blade element momentum theory (BEMT) approach described in [17, 18], which is implemented in an in-house code. The sectional distribution of lift and drag, along with the blade and hub geometry,

is specifically derived at this step. In the third step, noise source spheres are calculated by employing the Hanson frequency domain formulation [3, 17] that accounts for acoustic effects of varying α_{disk} and V. The second and third steps correspond to the two primary modules of a low-order propeller noise prediction solver (LOPNOR). This solver calculates tonal noise resulting from steady aerodynamic forces and blade geometry. The LOPNOR solver has been validated against high-fidelity CFD simulation and outdoor flyover noise measurements, covering constant altitude level flight and multiple take-off flights of a full-electric propeller-driven aircraft [17]. In this study, the solver is extended to calculate noise from multiple rotors, each potentially having different operational characteristics, without considering aerodynamic interactions between rotors. Noise from each rotor is computed individually, and the contributions of all rotors are then determined by summing their contributions incoherently at microphones distributed across a noise sphere surrounding the vehicle. This noise sphere is then utilized as input for the propagation and footprint calculation module.

Finally, the noise signals stored on the noise sphere are propagated in a 3D vertiport environment, and the corresponding noise footprint on the terrain surfaces is calculated using the beam tracing solver UYGUR [18–20]. A schematic illustration of the computational procedures is shown in Fig. 1, and its modules are described in more detail in the following.

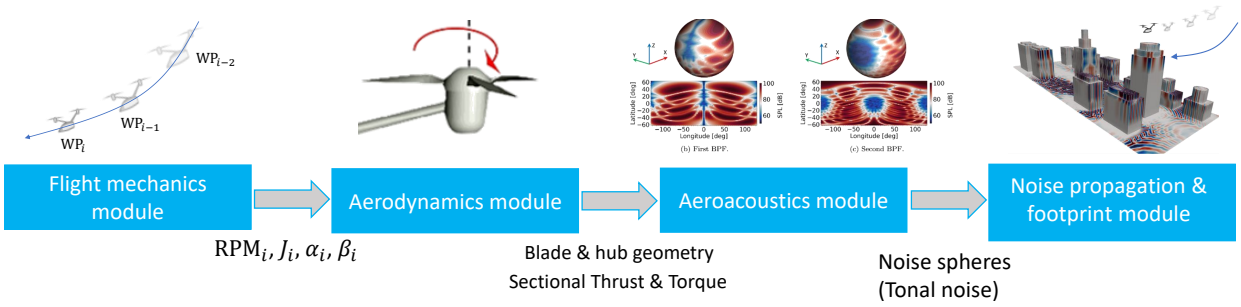

Fig. 1 A schematic illustration of the computational procedures.

A. Flight mechanics model

The trajectory of the aircraft is calculated by leveraging optimal control theory [21–23]. In this context, solving an optimal control problem means finding the trajectory that minimizes a specified cost function $\mathcal{J}$, which depends on the evolution in time of all flight parameters involved. The cost function is typically chosen to reflect the mission objectives, and can include the time of flight, the vehicle's fuel (or energy) consumption, or a combination of relevant performance metrics. The top-level characteristics of the maneuver which is desired to obtain are formulated as path constraints, bounds, equality and/or inequality constraints for a set of relevant flight parameters. The equations of motion describe the behavior of the vehicle in the simulated scenario, and act as dynamic constraints for the optimal control solver.

The proposed approach has been developed for applications to an eVTOL quad-rotor aircraft, but is, in principle, independent of the aircraft configuration. The aircraft is regarded as a point-mass with constant weight and is restricted to fly symmetrically in a vertical plane. Earth is assumed flat, and the International Standard Atmosphere (ISA) model is adopted with no wind. In these assumptions, the equations of motion in the aircraft body axes (x-axis towards the nose, z-axis in the pilot head-to-feet direction) are written as in Eqs. 1–6.

$$m\,(\dot{u} + qw) = -W\sin\theta_{\text{f}} - D\cos\alpha_{\text{f}} \tag{1}$$

$$m\,(\dot{w} - qu) = W\cos\theta_{\text{f}} - D\sin\alpha_{\text{f}} - \textstyle\sum_i T_i \tag{2}$$

$$I_y\dot{q} = \textstyle\sum_i T_i x_{T_i} \tag{3}$$

$$\dot{x}_E = V\cos\xi \tag{4}$$

$$\dot{h} = V\sin\xi \tag{5}$$

$$\dot{\theta}_f = q \tag{6}$$

The flight path angle ξ is positive for climbing flight. Following the convention typically used for fixed-wing aircraft, the aircraft pitch angle θ_{f} is positive for a nose-up attitude, and the angle of attack of the vehicle α_{f} (which equals the

propeller disk angle of attack α_{disk} in this work) is positive if the airspeed impinges on the lower side of the fuselage. The angle of attack is calculated as in Eq. 7, and linearly extrapolated with respect to time for the cases in which both u and w are zero, as it happens in hover.

$$\alpha_{\text{f}} = \theta_{\text{f}} - \xi = \arctan\left(\frac{w}{u}\right) \tag{7}$$

The airspeed V is calculated as in Eq. 8.

$$V = \sqrt{u^2 + w^2} \tag{8}$$

All rotors are assumed to be rigid and operating at the same rotational speed Ω, which is held constant throughout the maneuver in a similar way as done in [8]. The thrust produced by each rotor is assumed to be orthogonal to the rotor plane, and parallel to the aircraft vertical axis z. Thrust is expressed in terms of a thrust coefficient C_T according to Eq. 9, and its magnitude is controlled by a collective command $\theta_{0.75}$.

$$T_i = \pi\rho\Omega^2 R^4 C_{T_i}(\theta_{0.75}) \tag{9}$$

Aerodynamic drag D due to the aircraft fuselage is expressed in terms of dynamic pressure and equivalent skin-friction area A_{eq}, according to Eq. 10.

$$D = \frac{1}{2}\rho V^2 A_{\text{eq}} \tag{10}$$

Aerodynamic lift L due to the aircraft body is neglected for simplicity ($L = 0$), but its inclusion in the equations of motion as a function of the dynamic pressure and angle of attack does not affect the proposed methodology at any level.

The optimal control problem is formulated to find the time histories of the thrust coefficients $C_{T_i}(t)$ that result in a trajectory which minimizes the chosen cost function $\mathcal{J}$ while satisfying all imposed constraints. In an effort to obtain smooth evolutions of thrust, the control solver is made to find the optimal time histories of the derivatives of the thrust coefficients $\dot{C}_{T_i}(t)$, which are then integrated to obtain the thrust coefficients themselves. Such derivatives are bounded and penalized with an extra term in the cost function $\mathcal{J}_{\boldsymbol{u}}$, in a process which is sometimes referred to as "input damping" [24]. Once the evolution of the thrust coefficients is known, the induced velocity w_{in} at each rotor is estimated using Glauert's formula, shown in Eq. 11 [25]. This approach assumes that the inflow adapts instantaneously to the change of rotor thrust, and therefore neglects any inflow dynamics.

$$w_{\text{in}}: \; C_T = \frac{2w_{\text{in}}\sqrt{u^2 + (w + w_{\text{in}})^2}}{(\Omega R)^2} \tag{11}$$

The latter is then used to estimate the power coefficient C_{P_i} required by each rotor, which is expressed as in Eq. 12 using the integral results of BEMT [25].

$$C_P = C_T\sqrt{\frac{C_T}{2}}\left(\frac{K_{\text{in}}w_{\text{in}} + w}{\Omega R}\right) + \frac{\sigma C_d}{8}\left[1 + 4.65\left(\frac{u}{\Omega R}\right)^2\right] \tag{12}$$

The total power P required by the aircraft is then calculated as in Eq. 13.

$$P = DV + \sum_i \pi\rho\Omega^3 R^5 C_{P_i} \tag{13}$$

The collective angle $\theta_{0.75}$ required to generate the calculated combination of thrust coefficient and inflow velocity is estimated using Eq. 14, which is valid for rotors with constant chord and linear twist distributions along the radius [25]. To apply this formula, a mean chord and a linear approximation of the twist distribution of the original geometry presented in [26] have been used. The collective angle is measured with respect to the blade at the 75% radius station.

$$\theta_{0.75}: \; C_T = \frac{C_{l_\alpha}\sigma}{2}\left\{\frac{\theta_{0.75}}{3}\left[1 + \frac{3}{2}\left(\frac{u}{\Omega R}\right)^2\right] + \frac{\theta_{\text{tw}}}{4}\left[\left(\frac{u}{\Omega R}\right)^2 + 1\right] - \frac{1}{2}\left(\frac{w + w_{\text{in}}}{\Omega R}\right)\right\} \tag{14}$$

The time-histories of all flight parameters are sampled approximately every 0.5 s (depending on the final time elapsed during the maneuver) to calculate the aerodynamic and acoustic performance of the aircraft.

B. Aerodynamics model

The aerodynamic solver is initiated through a two-step process. Initially, the propeller blade geometry is read in the standard triangle language (STL) file format. Subsequently, the blade geometry is discretized along its span, extracting sectional airfoil coordinates and blade twist angle β at each blade section, following the XFOIL convention. This ensures direct compatibility with XFOIL without the need for manual modifications. Simultaneously, the flight trajectory is read as a sequence of N WPs, with i representing the index of WPs. At WP_i, corresponding parameters such as Ω_i, V_i, J_i, α_{disk} are retrieved from the flight trajectory.

At WP_i, the range of Reynolds numbers (R_e) that cover the entire radial variation is estimated based on V_i and the distribution of blade chords across the blade radius. This process generates several R_e values covering the entire radial variation. The range of α_b extends from $-16°$ to $16°$ with a $2°$ increment. Following this, XFOIL is internally executed for the specified R_e and α_b, generating a 2D mesh of sectional lift and drag coefficients denoted as $C_l(Re, \alpha_b)$ and $C_d(Re, \alpha_b)$, respectively. Post-stall lift and drag coefficients are determined using the Viterna & Corrigan approach [27].

In the second step, the BEMT procedure determines the sectional lift and drag along the blade radius. Specifically, within the BEMT procedure, the sectional lift and drag on an annulus of width Δr are determined by establishing an equilibrium. This equilibrium reads:

$$\Delta T = 4\pi R\rho V^2(1+a)a\Delta r = \frac{1}{2}\rho_\infty V_1^2 b_c(C_l\cos\phi - C_d\sin\phi)B\Delta r, \tag{15}$$

$$\Delta Q = 4\pi R^3\rho V\Omega(1+a)b\Delta r = \frac{1}{2}\rho_\infty V_1^2 b_c(C_d\cos\phi + C_l\sin\phi)BR\Delta r, \tag{16}$$

where R is the radius of current blade section and b_c is the blade sectional chord, B is the number of blades, a and b are the axial and azimuthal velocity induction coefficients. These coefficients correlate with the axial and tangential velocities, expressed as $V_x = V_\infty(1+a)$ and $V_t = \Omega R(1-b)$. The total velocity seen by an airfoil at a radial section is given by $V_1 = \sqrt{V_x^2 + V_t^2}$. The flow induction angle ϕ, is defined as $\tan^{-1}(V_x/V_t)$. The local angle of attack α_b at a blade section is determined by the relation $\alpha_b = \beta - \phi$. Simultaneously, the local Reynolds number R_e at the blade section is calculated using V_1 and b_c. The corresponding lift and drag coefficients C_l and C_d at the sectional airfoil are then interpolated from pre-computed 2D meshes of $C_l(Re, \alpha_b)$ and $C_d(Re, \alpha_b)$ and are delivered to inputs, together with the respective blade sectional areas, for the acoustic calculation. Additional details on the aerodynamic solver can be found in [17].

C. Aeroacoustics model

The frequency domain acoustic formulation derived by Hanson [3] that accounts for the acoustic effect of non-zero α_{disk} is employed in this work. The loading $p'_L(\boldsymbol{x}, \Omega)$ and thickness $p'_T(\boldsymbol{x}, \Omega)$ components of the tonal noise read

$$p'_L(\boldsymbol{x}, \Omega) = \frac{i\rho cBe^{ik_m S}}{4\pi(S/r_t)(1 - M_x\cos\theta)} \sum_{k=-\infty}^{\infty} e^{i(mB-k)(\phi'-\pi/2)} \times \int_0^{r_t} M_r^2 \hat{\Psi}_{Fk}(k_x) J_{mB-k}\left(\frac{mBz_0 M_r \sin\theta'}{1 - M_x\cos\theta}\right) dz_0, \tag{17}$$

$$p'_T(\boldsymbol{x}, \Omega) = \frac{-\rho c^2 Be^{ik_m S}}{4\pi(S/r_t)(1 - M_x\cos\theta)} \sum_{k=-\infty}^{\infty} e^{i(mB-k)(\phi'-\pi/2)} \times \int_0^{r_t} M_r^2 \hat{k_x}^2 t_b \hat{\Psi}_V(\hat{k_x}) J_{mB-k}\left(\frac{mBz_0 M_r \sin\theta'}{1 - M_x\cos\theta}\right) dz_0. \tag{18}$$

where the angles θ' and ϕ' are given by the following relations with respect to α_{disk} [3, 28]

$$\cos\theta' = \cos\theta\cos\alpha_{disk} + \sin\theta\sin\phi\sin\alpha_{disk}, \tag{19}$$

$$\cos\phi' = \frac{\sin\theta}{\sin\theta'}\cos\phi. \tag{20}$$

The frequency domain source function is expressed as $\hat{\Psi}_{Fk}$, and it can be written in various forms. This work considers an expression of $\hat{\Psi}_{Fk}$ that is explicitly dependent on the aerodynamic coefficients, as advised by Hanson [3].

$$\hat{\Psi}_{Fk} = \frac{1}{2}(k_y C_{lk}\hat{\Psi}_{lk} + k_x C_{dk}\hat{\Psi}_{dk}). \tag{21}$$

$\hat{\Psi}_{Fk}$ is associated with the source functions Ψ, as previously elucidated by Hanson [29], through the following relation

$$\hat{\Psi}_{(\cdot)k} = \Psi_{(\cdot)k} e^{i(\phi_s + \phi_{FA})}, \tag{22}$$

where ϕ_s is the phase angle due to sweep and ϕ_{FA} is the phase shift associated with Face Alignment. In this study, parabolic thickness distribution and uniform lift distribution, as defined by Eq. (16)-(17) in Kotwicz Herniczek et al. [28], are utilized, following the recommendation of Magliozzi et al. [30]. The dimensionless wave numbers k_x and k_y, representing chordwise and spanwise dimensions, respectively, are determined according to Hanson [29]

$$k_x = \frac{2mBM_t}{M_r(1 - M_x \cos\theta)} B_D, \quad k_y = \frac{2mB}{2M_r} \left(\frac{M_r^2 \cos\theta - M_x}{1 - M_x \cos\theta} \right) B_D. \tag{23}$$

The wavenumber $\hat{k_x}$ in Eq. 18 reads

$$\hat{k_x} = 2 \left(\frac{mB - k}{z_0} \cos\zeta + \frac{mBM_r \cos\theta'}{1 - M_x \cos\theta} \sin\zeta \right) B_D \tag{24}$$

where ζ is the helix angle which varies along the blade span. In a previous study by Hanson [29], the angle was denoted as the advance helix. However, Hanson argued in a subsequent study [3] that it could alternatively represent the blade twist angle or any other pertinent angle that varies along the blade span and is associated with the distribution of noise sources. In this study, the helix angle ζ is specifically set to the blade twist angle β. Furthermore, solely steady loading and thickness noise are considered, encompassing only the zeroth harmonic of loading ($k = 0$).

D. Noise propagation and footprint prediction model

The noise propagation and footprint calculation solver utilizes the Gaussian beam propagation solver UYGUR [18–20]. Input parameters include the noise sphere, terrain geometries, and environmental profiles encompassing wind and temperature distributions across the computational domain. The solver produces noise levels in sound pressure level (SPL) on the terrain surfaces. Further information about this solver is available in [18–20].

III. Case study

A. Aircraft model

The single-passenger eVTOL quad-rotor aircraft described in [31] is used as the subject of applications presented in this work, and is depicted in Fig. 2. It is propelled by four identical three-bladed rotors, with each rotor blade featuring the twist angle and chord distributions proposed in [26]. Because the analyses is limited to symmetric flight, the two front rotors are assumed to operate at the same conditions, and the same holds for the two rear rotors. The top-level characteristics of the aircraft and rotors are summarized in Tables 1 and 2.

Table 1 Aircraft and rotor geometric parameters, extracted or estimated from [26, 31]

	m	I_y	R	A_{eq}	σ	θ_{tw}	$x_{T_{\text{fr}}}$	$x_{T_{\text{re}}}$	$z_{T_{\text{fr}}}$	$z_{T_{\text{re}}}$
Value	455	1600	1.92	0.32	0.145	−41.5	2.39	−2.79	−1.73	−2.40
Unit	kg	kg m^2	m	m^2	-	°/m	m	m	m	m

Table 2 Aircraft and rotor performance parameters, extracted or estimated from [26, 31]

	V_{cr}	Ω	C_{l_α}	C_d	K_{in}	$C_{T_{\text{max}}}$	P_{max}
Value	36.5	716	0.104	128	1.15	3.17×10^{-2}	64400
Unit	m/s	rpm	1/°	counts	-	-	W

The noise sphere is positioned at the center of gravity and sphere radius is set to $24R$ to satisfy the acoustic far-field condition, which ensures that the acoustic field remains unaffected by the flow field.

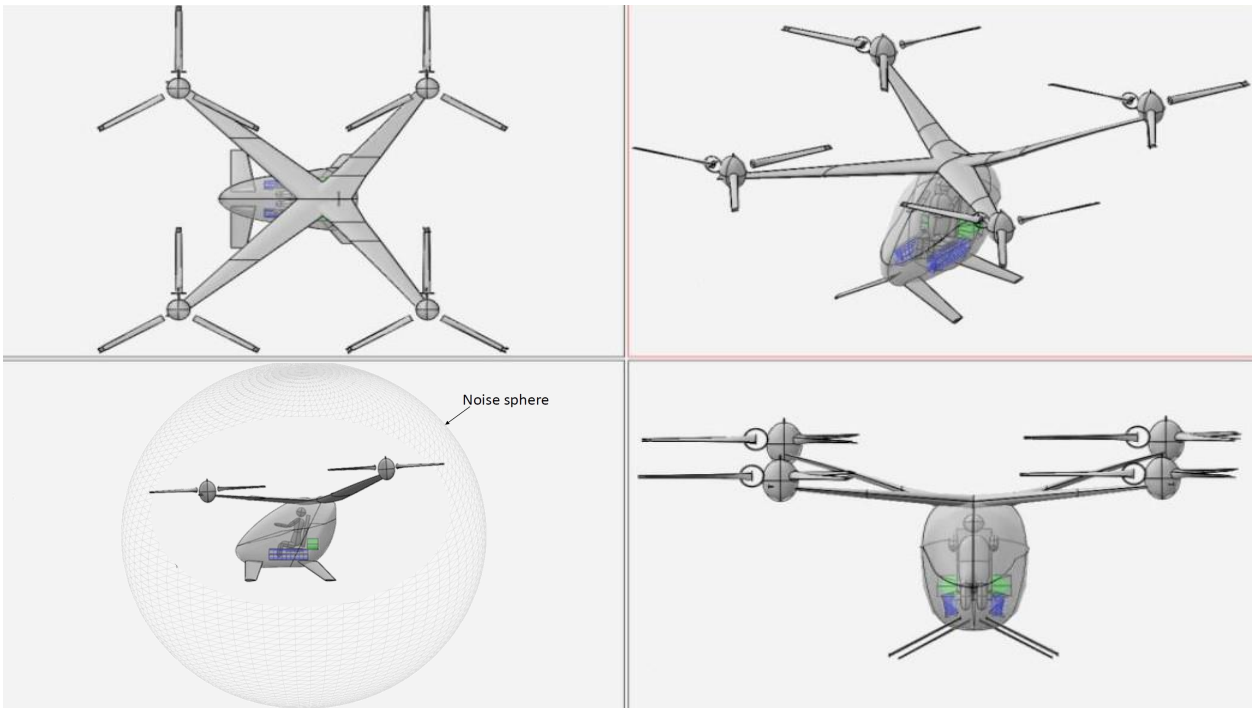

Fig. 2 Geometry of the eVTOL vehicle and the noise sphere used in this work [31]

B. Trajectories

Two trajectories are obtained by means of the optimal control solver to serve as inputs for the aero-acoustic analysis. The first is a minimum-time deceleration at constant altitude, from cruise speed to hover conditions. The second is a minimum-time acceleration at constant altitude, from hover conditions to cruise speed. They are representative of simple approach and departure procedures for eVTOL vehicles in an abstract scenario.

In both cases, the aircraft flies in the positive direction of the x_E axis, at a constant altitude of $h = 200\,\mathrm{m}$ above ground. The approach trajectory starts in cruise conditions at $x_E < 0$, and ends at $x_E = 0$ in hover conditions. In this case, the initial position is left free for the optimal control solver to determine. The departure trajectory starts in hover conditions at $x_E = 0$ and accelerates until cruise speed is reached at $x_E > 0$. In this case, the final position is left free for the optimal control solver to determine. In order to stimulate aggressive variations of the pitch angle, both maneuvers are executed in the minimum time, according to the cost function expressed as in Eq. 25.

$$\mathcal{J} = t_{\mathrm{fin}} \left[1 + \int_0^{t_{\mathrm{fin}}} \left(\dot{C}^2_{T_{\mathrm{fr}}} + \dot{C}^2_{T_{\mathrm{re}}} \right) \mathrm{d}t \right] \tag{25}$$

To impose steady-state initial and final conditions for both the approach and departure optimal control problems, the aircraft is trimmed for cruise or hover by solving Eqs. 26, which are obtained by imposing $\dot{u} = \dot{w} = \dot{q} = q = \xi = 0$ in Eqs. 1-3.

$$\theta_{\mathrm{f}} = \arctan\left(-\frac{D}{W}\right) \quad \Rightarrow \quad T_{\mathrm{fr}} = \frac{W\cos\theta_{\mathrm{f}} - D\sin\theta_{\mathrm{f}}}{1 - x_{T_{\mathrm{fr}}}/x_{T_{\mathrm{re}}}} \quad \Rightarrow \quad T_{\mathrm{re}} = -T_{\mathrm{fr}}\frac{x_{T_{\mathrm{fr}}}}{x_{T_{\mathrm{re}}}} \tag{26}$$

The most relevant flight parameters are bounded as in Table 3. An additional non-linear terminal constraint ensures that the final instant is reached in steady-state conditions ($\dot{u} = \dot{w} = \dot{q} = 0$), and a path constraint ensures that the power available is always greater than the power required by the aircraft.

The optimal control problems are solved by using the direct collocation method provided by the ICLOCS2* open-source toolbox, adopting a Hermite-Simpson discretization scheme and employing the IPOPT† (Interior Point OPTimizer) non-linear programming solver [32, 33]. The resulting trajectories are shown in Fig. 3 with respect to

*http://www.ee.ic.ac.uk/ICLOCS/Overview.html

†https://coin-or.github.io/Ipopt/

Table 3 Flight parameter bounds

	u	w	q	h	θ_f	$C_{T_{\text{fr}}}$	$C_{T_{\text{re}}}$	$\dot{C}_{T_{\text{fr}}}$	$\dot{C}_{T_{\text{fr}}}$
Lower bound	−40	−40	−10	200	−15	0	0	-5×10^{-4}	-5×10^{-4}
Upper bound	40	40	10	200	15	$C_{T_{\text{max}}}$	$C_{T_{\text{max}}}$	5×10^{-4}	5×10^{-4}
Unit	m/s	m/s	°/s	m	°	–	–	1/s	1/s

distance covered along the x_E axis. It can be seen that in steady-state conditions (initial and final condition of each maneuver), the front rotors are required to generate more thrust than the rear rotors, since they lie closer to the center of mass of the vehicle. The aircraft accelerates and decelerates by tilting the resultant thrust vector forward or backward, which is achieved by applying differential thrust in the transient phases of the maneuvers. The maneuvers are performed in the minimum time by aggressively pitching the aircraft up or down, until the imposed limit pitch angle of ±15° is reached. This is the limiting constraint in the execution of the maneuver, since the aircraft remains safely within the imposed performance limits on $C_{T_{\text{max}}}$ and $C_{P_{\text{max}}}$. The final time for the approach maneuver is $t_{\text{fin}} = 15.47$ s. The final time for the departure maneuver is $t_{\text{fin}} = 17.27$ s.

C. Vertiport environment

The vertiport is installed on the rooftop of a high-rise building within an urban setting previously utilized in a study by the lead author [20], where it is elaborated further. In this investigation, the X and Y coordinates of the vertiport are repositioned to $X = 0$ m and $Y = 0$ m, respectively, with the vertiport situated at a height of 130 m. The ground surface extends along the X-axis from 100 m to 500 m, as depicted in Fig. 4. The atmosphere is considered quiescent, maintaining a constant temperature of 22 °C, while the terrain surface is regarded as an acoustically rigid wall, thus functioning as a perfect reflector.

D. Description of test cases

In this study, instead of calculating the noise footprint at each WP within the flight trajectory, noise footprints from several representative WPs exhibiting significant variations in α_{disk} and V_∞ were considered. To achieve this, WPs corresponding to the flight mission times at $t = 2.5$s, 13s in the approach trajectory, as well as 2.5s and 15s in the departure trajectory were specifically chosen and denoted as A, B, C, and D as illustrated in Fig. 4. The source positions and associated flight parameters required for aerodynamic and aeroacoustic calculations are extracted from those WPs and listed in Table 4. As the eVTOL fuselage does not significantly affect acoustics for this specific vehicle geometry [34], and the rotors are the primary noise source, noise scattered by the airframes was neglected. Case 1 is characterized by high-speed forward flight with the nose up, while Case 3 depicts a flight scenario with low speed and the nose down, and Case 4 entails high-speed forward flight with the nose down. Case 2, serving as a reference, features near-hover conditions against which the acoustic effects of variations in forward flight speed V and vehicle pitch angle α_{disk} represented by Cases 1, 3, and 4 will be investigated. All cases are run on an Intel(R) Xeon(R) Gold 6140 GPU 2.3 GHz processor with 36 cores.

Table 4 Test matrix for the case study.

Case #	trajectory type	t (s)	V (m/s)	α (deg)	$C_{T_{\text{fr}}}$	$C_{T_{\text{re}}}$	WP (m)
1	approach	2.5	32.8	15	0.004573	0.003431	A = (-180.4, 0, 200)
2	approach	13	3.6	0	0.004632	0.003372	B = (-2.7, 0, 200)
3	departure	2.5	3.3	-15	0.004604	0.003397	C = (2.38, 0, 200)
3	departure	15	33.7	-15	0.004632	0.003365	D = (240.31, 0, 200)

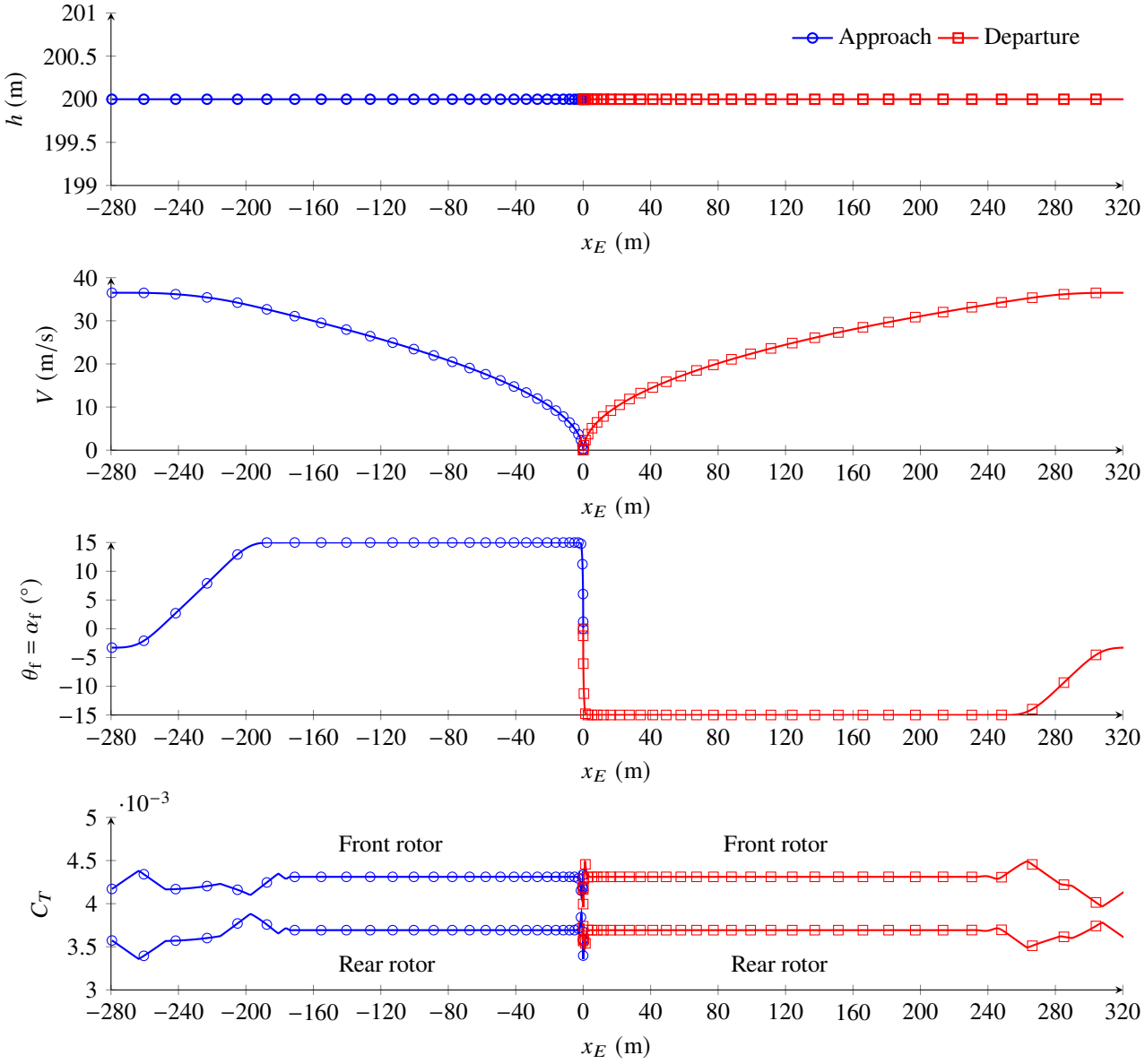

Fig. 3 Evolution of flight parameters during approach and departure maneuvers.

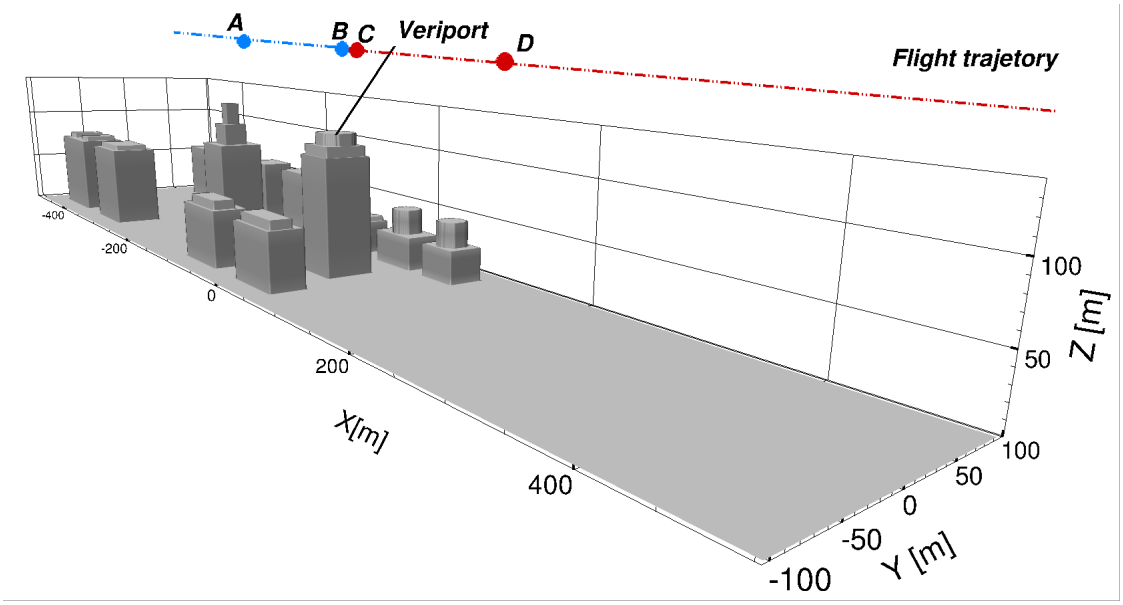

Fig. 4 Illustration of the urban vertiport environment geometry, showcasing the approach trajectory depicted by a blue line and the departure trajectory represented by a red curve.

.

E. Results

1. Noise spheres

The noise spheres, corresponding to the first harmonics of blade passing frequency (BPF), are calculated for all Cases utilizing the LOPNOR tool [17], which encompasses the aerodynamic and acoustic solvers outlined in Section II. These noise spheres are illustrated in Fig. 5. To highlight the acoustic effect of non-zero α_{disk}, variations in noise levels are examined at two specific locations on the noise spheres. Region F, located closer to the vehicle's front, and region R, closer to the rear rotors, are selected, as shown in Fig. 5a.

When the vehicle is pitched up, as in Case 1, noise levels intensify and shift toward lower regions of the noise sphere compared to Case 2, except in region F where noise levels shift upwards. The significant increase in noise levels is attributed to the higher flight velocity in Case 1, while the shift in noise levels towards lower regions of the noise sphere is attributed to the vehicle pitch angle α_{disk}. This trend aligns with previous works mentioned in Section I. It is noteworthy that when the vehicle pitches up, noise levels in region F are shifted upwards, with increases observed above a point at Longitude 0° and Latitude 0°, in contrast to the trends observed in other regions of the noise sphere.

Conversely, when the vehicle pitches down, as in Case 3, noise levels slightly increase and shift towards upper regions of the noise sphere, except in region F where noise levels shift downwards compared to Case 2. This slight increase in noise levels is likely attributed to the variation in α_{disk}, as the flight speed remains almost the same between Case 3 and Case 2. When the flight speed is increased while the vehicle pitches down, as in Case 4, the trend observed in Case 3 is further emphasized, with noise levels in the upper regions of the noise sphere increasing due to flight speed, while a slight rise in noise levels in the lower regions of the noise sphere is also noted.

The aforementioned observation highlights the significant alteration in the directivity of the noise source due to variation in α_{disk}, while noise radiation is amplified by variations in flight speed, irrespective of whether the vehicle is pitched up or down. The subsequent analysis investigates the acoustic effects of variations in V and α_{disk} on the instantaneous noise footprint.

2. Instantaneous noise footprints

The evaluation of the acoustic impact of varying V on the noise footprint is conducted by comparing noise footprints between Case 1 and Case 2 for the approach trajectory, and between Case 3 and Case 4 for the departure trajectory. Instantaneous noise footprints for all Cases were computed and illustrated in Fig. 6. A notable increase in the noise

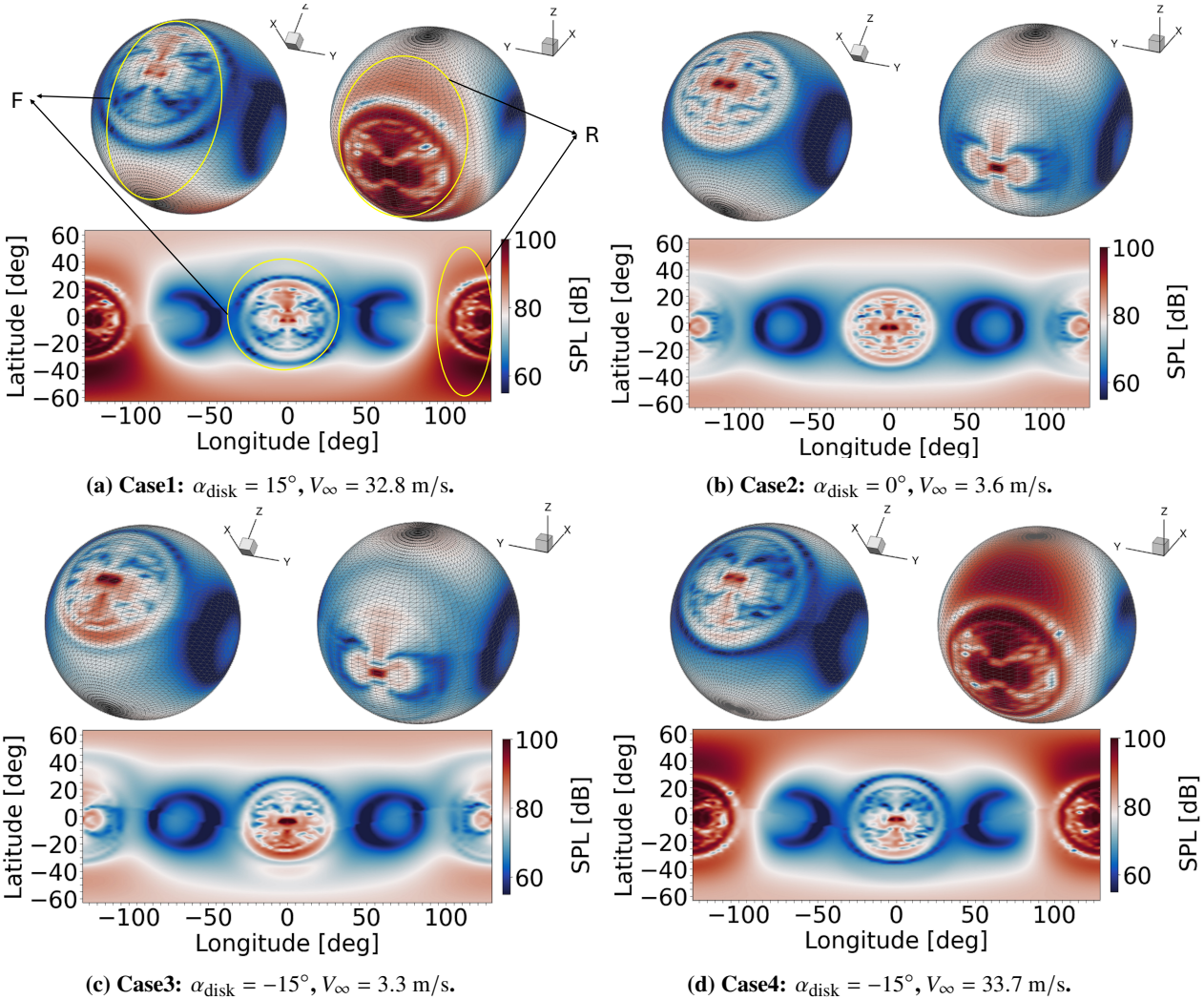

(a) Case1: $\alpha_{\text{disk}} = 15°$, $V_\infty = 32.8$ m/s.

(b) Case2: $\alpha_{\text{disk}} = 0°$, $V_\infty = 3.6$ m/s.

(c) Case3: $\alpha_{\text{disk}} = -15°$, $V_\infty = 3.3$ m/s.

(d) Case4: $\alpha_{\text{disk}} = -15°$, $V_\infty = 33.7$ m/s.

Fig. 5 Noise spheres computed for the first BPF. The vehicle's orientation is defined with the nose pointing towards the positive X-axis.

footprint directly below the source position in the building area is observed compared to Case 2. This increase is attributed to the pitch-up motion of the vehicle, which effectively directs noise towards the lower region of the source sphere, as elaborated in the preceding section. The comparison of noise footprints from Cases 1-2 highlights that a significant increase in on-ground noise levels can be expected when the vehicle performs nose-up during the approach maneuver toward the vertiport, especially if the vehicle speed is high. The impact of flight speed on the noise footprint is also evident in the noise footprints computed for Case 3 and Case 4. Namely, as flight speed V increases, on-ground noise levels are raised accordingly regardless of whether the vehicle pitches up or down. The observed trend suggests that lower flight speed during approach and departure maneuvers is desirable to decrease the noise footprint.

The acoustic effect of varying α_{disk} is investigated by comparing noise footprints computed for Case 1 and Case 3 against the one computed for Case 2. When the vehicle is nose up, as in Case 1, higher noise levels are observed at receivers distributed in the building areas that is directly below the source. This is directly associated to the source directivity pattern as observed in Fig. 5a, noise radiation intensifies around the lower regions of the noise sphere due to nose up manuevere of the vehicle. Simultaneously, a considerable reduction in the noise footprint in the flat region far behind the building areas was noted. This reduction can be attributed to two primary factors. Firstly, due to source directivity in region F, higher noise levels are shifted upward, while lower levels are observed below the point at Longitude 0° and Latitude 0°, as depicted in Fig. 5a. Consequently, as the vehicle pitches up, these lower noise levels are directed to the flat region of the urban area. Secondly, building blocks shield incoming noise field, further diminishing noise far behind the building areas. However, at lower frequencies, this shielding mechanism may be less effective due to sound waves diffracted by the building edges, as discussed in [20].

When the vehicle pitches down, as in Case 3, on-ground noise levels decrease within a region directly beneath the source, denoted by X=[-500,-250] m and Y=[-100,100] m. This decrease is attributed to reduced efficiency in noise radiation towards the ground due to the downward pitch motion of the vehicle. Consequently, noise predominantly radiates around the upper region of the source sphere, as illustrated in Fig. 5c. Conversely, a significant increase in noise levels, by 10 dB, occurs in the flat region bounded by X=[200,400] m and Y=[-100,100] m. The observed increase is ascribed to alterations in source directivity within region F of the source sphere, leading to a downward shift in higher noise levels, while lower levels are noted above in relation to the point at Longitude 0° and Latitude 0°, as illustrated in Fig. 5c in comparison to Case 2. Overall, variations in α_{disk} significantly influence noise radiation directivity: when the vehicle pitches up, on-ground noise levels beneath the source increase, while those at receivers farther away decrease; conversely, when the vehicle pitches down, on-ground noise levels beneath the source decrease, while those at receivers farther away increase.

IV. Conclusions and Future Work

This work proposes a novel methodology to predict the instantaneous noise footprint of UAM maneuvers around a vertiport installed on the rooftop of a high-rise building. The methodology integrates various models encompassing flight mechanics, aerodynamics, aeroacoustics, noise propagation, and footprint calculation. The approach is applied to assess the instantaneous noise footprints generated during both approach and departure flights of a quad-rotor vehicle. Emphasis is placed on the acoustic impacts resulting from variations in vehicle flight speed V and vehicle pitch angle α_{disk} by comparing noise footprints computed for various Waypoints (WPs) exhibiting notable differences in V and α_{disk}.

The comparison of noise footprints from all selected WPs suggest that as flight speed V increases, on-ground noise levels are raised accordingly regardless of whether the vehicle pitches up or down. The observed trend indicates that lower flight speed during approach and departure maneuvers is desirable to decrease the noise footprint. Overall, high-speed approach or departure is not desired. It is also shown that variations in α_{disk} significantly influence noise radiation directivity: when the vehicle pitches up, on-ground noise levels beneath the source increase, while those at receivers farther away decrease; conversely, when the vehicle pitches down, on-ground noise levels beneath the source decrease, while those at receivers farther away increase. It is also found that the building blocks further shield the incoming noise and further decrease the noise levels at receivers distributed behind the building blocks.

While valuable insights are offered into efficiently evaluating instantaneous noise footprints of UAM flight procedures in vertiport environments, limitations at the current stage must be acknowledged. The thrust calculation and BEMT aerodynamic module are constrained by assumptions on uniform inflow condition, thus neglecting the unsteady loading due to variation in α_{disk} and its acoustic contribution. Future work will address this limitation with an appropriate aerodynamic model allowing calculation of unsteady loading due to non-zero α_{disk}, and will introduce the impact of rotors' induced velocity in thrust calculation. These enhancements, while minor, may yield more realistic figures of merit for noise footprint evaluation. Overall, the necessity of the proposed approach in evaluating UAM flight trajectory

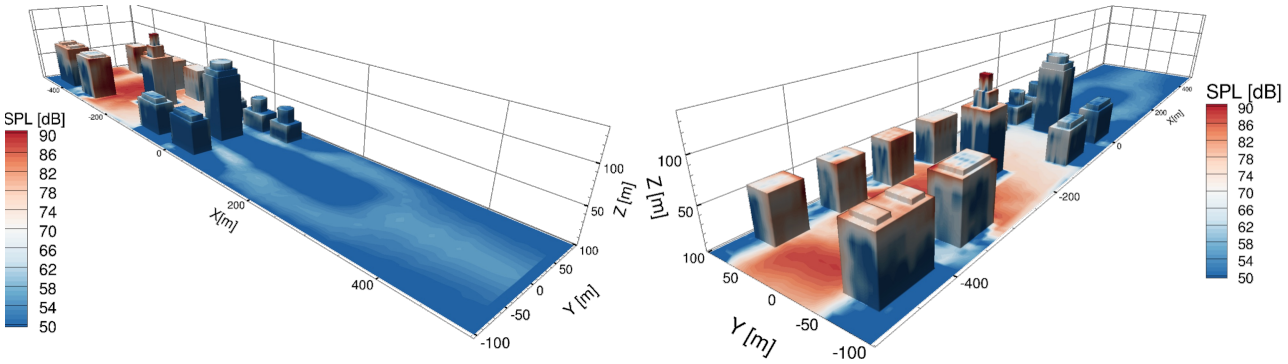

(a) Case1: $\alpha_{\text{disk}} = 15°$, $V_\infty = 32.8$ m/s**, source position at WP A = (-180.4, 0, 200)** m.

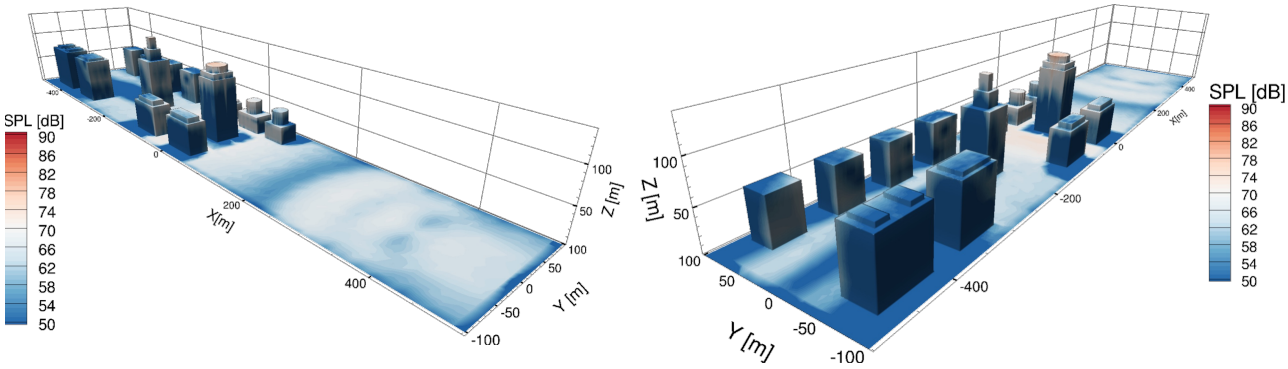

(b) Case2: $\alpha_{\text{disk}} = 0°$, $V_\infty = 3.6$ m/s**, source position at WP B = (-2.7, 0, 200)** m.

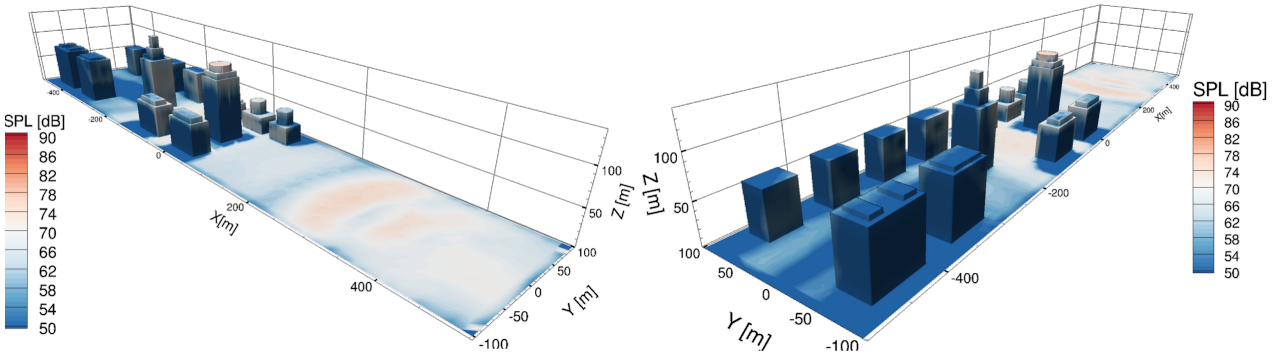

(c) Case3: $\alpha_{\text{disk}} = -15°$, $V_\infty = 3.3$ m/s**, source position at WP C = (2.38, 0, 200)** m.

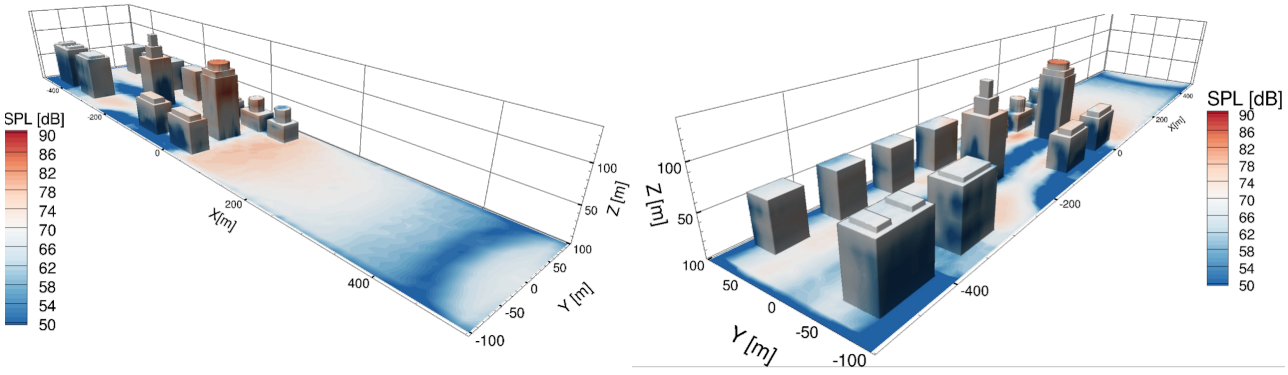

(d) Case4: $\alpha_{\text{disk}} = -15°$, $V_\infty = 33.7$ m/s**, source position at WP D = (240.31, 0, 200)** m.

Fig. 6 Instantaneous noise footprints. Vertiport location (0, 0, 130) m.

noise footprints in vertiport environments is underscored, providing valuable insights for early design stages.

References

[1] Schweiger, K., and Preis, L., "Urban air mobility: Systematic review of scientific publications and regulations for vertiport design and operations," *Drones*, Vol. 6, No. 7, 2022, p. 179.

[2] Mani, R., "The radiation of sound from a propeller at angle of attack," *Proceedings of the Royal Society of London. Series A: Mathematical and Physical Sciences*, Vol. 431, No. 1882, 1990, pp. 203–218.

[3] Hanson, D., "Noise radiation of propeller loading sources with angular inflow," *13th Aeroacoustics Conference*, 1990, p. 3955.

[4] KREJSA, E., "Prediction of the noise from a propeller at angle of attack," *13th aeroacoustics conference*, 1990, p. 3954.

[5] Hanson, D. B., "Direct frequency domain calculation of open rotor noise," *AIAA journal*, Vol. 30, No. 9, 1992, pp. 2334–2337.

[6] Envia, E., "Prediction of noise field of a propfan at angle of attack," *Unsteady aerodynamics, aeroacoustics, and aeroelasticity of turbomachines and propellers*, Springer, 1993, pp. 685–703.

[7] Carley, M., "The structure of wobbling sound fields," *Journal of sound and vibration*, Vol. 244, No. 1, 2001, pp. 1–19.

[8] Casalino, D., van der Velden, W. C., and Romani, G., "Community noise of urban air transportation vehicles," *AIAA Scitech 2019 Forum*, 2019, p. 1834.

[9] Hanson, D., "Sound from a propeller at angle of attack: a new theoretical viewpoint," *Proceedings of the Royal Society of London. Series A: Mathematical and Physical Sciences*, Vol. 449, No. 1936, 1995, pp. 315–328.

[10] Romani, G., Grande, E., Avallone, F., Ragni, D., and Casalino, D., "Computational study of flow incidence effects on the aeroacoustics of low blade-tip Mach number propellers," *Aerospace Science and Technology*, Vol. 120, 2022, p. 107275.

[11] Goyal, J., Sinnige, T., Ferreira, C. S., and Avallone, F., "Aerodynamics and Far-field Noise Emissions of a Propeller in Positive and Negative Thrust Regimes at Non-zero Angles of Attack," *AIAA AVIATION 2023 Forum*, 2023, p. 3217.

[12] Yunus, F., Casalino, D., Avallone, F., and Ragni, D., "Toward inclusion of atmospheric effects in the aircraft community noise predictions," *The Journal of the Acoustical Society of America*, Vol. 150, No. 2, 2021, pp. 759–768.

[13] Hanson, D. B., and Parzych, D. J., "Theory for noise of propellers in angular inflow with parametric studies and experimental verification," Tech. rep., 1993.

[14] Yunus, F., Romani, G., Casalino, D., and Mirjam, S., "Efficient Prediction of Noise Emission from a Propeller Operating at Non-Zero Angle of Attack," *Quiet Drones Symposium 2024*, 2024.

[15] Ghorbaniasl, G., and Lacor, C., "A moving medium formulation for prediction of propeller noise at incidence," *Journal of Sound and Vibration*, Vol. 331, No. 1, 2012, pp. 117–137.

[16] Ghorbaniasl, G., Huang, Z., Siozos-Rousoulis, L., and Lacor, C., "Analytical acoustic pressure gradient prediction for moving medium problems," *Proceedings of the Royal Society A: Mathematical, Physical and Engineering Sciences*, Vol. 471, No. 2184, 2015, p. 20150342.

[17] Yunus, F., von den Hoff, B., and Snellen, M., "Predicting tonal noise of full-electric propeller-driven aircraft in outdoor environments using low-order models," *30th AIAA/CEAS Aeroacoustics 2024 Conference*, 2024.

[18] Yunus, F., "Methodologies and algorithms for sound propagation in complex environments with application to urban air mobility: A ray acoustics approach," PhD thesis, Delft University of Technology, Delft, The Netherlands, September 2023. Available at `https://research.tudelft.nl/en/publications/methodologies-and-algorithms-for-sound-propagation-in-complex-env`.

[19] Yunus, F., Casalino, D., Avallone, F., and Ragni, D., "Efficient prediction of airborne noise propagation in a non-turbulent urban environment using Gaussian beam tracing method," *The Journal of the Acoustical Society of America*, Vol. 153, No. 4, 2023, pp. 2362–2362.

[20] Yunus, F., Casalino, D., Avallone, F., and Ragni, D., "Efficient prediction of urban air mobility noise in a vertiport environment," *Aerospace Science and Technology*, Vol. 139, 2023, p. 108410.

[21] Kirk, D. E., *Optimal control theory: an introduction*, Dover Publications, Mineola, N.Y, 2004.

[22] Hull, D. G., *Optimal Control Theory for Applications*, Springer New York, 2003. https://doi.org/10.1007/978-1-4757-4180-3, URL http://dx.doi.org/10.1007/978-1-4757-4180-3.

[23] Bryson, A. E., and Ho, Y.-C., *Applied Optimal Control: Optimization, Estimation, and Control*, Routledge, 2018. https://doi.org/10.1201/9781315137667, URL http://dx.doi.org/10.1201/9781315137667.

[24] Hartjes, S., "An Optimal Control Approach to Helicopter Noise and Emissions Abatement Terminal Procedures," Ph.D. thesis, Delft University of Technology, 2015. https://doi.org/10.4233/UUID:CA4B93AC-6A39-4C89-8699-E0A351E7FE2F, URL http://resolver.tudelft.nl/uuid:ca4b93ac-6a39-4c89-8699-e0a351e7fe2f.

[25] Johnson, W., *Rotorcraft Aeromechanics*, Cambridge University Press, 2013. https://doi.org/10.1017/cbo9781139235655, URL http://dx.doi.org/10.1017/cbo9781139235655.

[26] Casalino, D., Grande, E., Romani, G., Ragni, D., and Avallone, F., "Definition of a benchmark for low Reynolds number propeller aeroacoustics," *Aerospace Science and Technology*, Vol. 113, 2021, p. 106707.

[27] Viterna, L., and Corrigan, R., "Fixed pitch rotor performance of large horizontal axis wind turbines,N83 19233,1981," Tech. rep., NASA, 1981.

[28] Kotwicz Herniczek, M. T., Feszty, D., Meslioui, S.-A., and Park, J., "Applicability of early acoustic theory for modern propeller design," *23rd aiaa/ceas aeroacoustics conference*, 2017, p. 3865.

[29] Hanson, D. B., "Helicoidal surface theory for harmonic noise of propellers in the far field," *AIAA journal*, Vol. 18, No. 10, 1980, pp. 1213–1220.

[30] Magliozzi, B., Hanson, D., and Amiet, R., "Propeller and propfan noise," *Aeroacoustics of flight vehicles: theory and practice*, Vol. 1, 1991, pp. 1–64.

[31] Johnson, W., Silva, C., and Solis, E., "Concept vehicles for VTOL air taxi operations," *AHS Specialists"Conference on Aeromechanics Design for Transformative Vertical Flight*, 2018.

[32] Wächter, A., and Biegler, L. T., "Line Search Filter Methods for Nonlinear Programming: Motivation and Global Convergence," *SIAM Journal on Optimization*, Vol. 16, No. 1, 2005, p. 1–31. https://doi.org/10.1137/s1052623403426556, URL http://dx.doi.org/10.1137/S1052623403426556.

[33] Wächter, A., and Biegler, L. T., "Line Search Filter Methods for Nonlinear Programming: Local Convergence," *SIAM Journal on Optimization*, Vol. 16, No. 1, 2005, p. 32–48. https://doi.org/10.1137/s1052623403426544, URL http://dx.doi.org/10.1137/S1052623403426544.

[34] Jia, Z., and Lee, S., "Acoustic analysis of a quadrotor eVTOL design via high-fidelity simulations," *25th AIAA/CEAS Aeroacoustics Conference*, 2019, p. 2631.